Two-transition-metal water oxidation catalysts. Faster rates via electronic structure tuning

Craig Hill (chill@emory.edu)
Emory University https://orcid.org/0000-0002-5506-9588
Meilin Tao
Emory University
Qiushi Yin
Emory University
Alexey Kaledin
Emory University
Natalie Uhlikova
Emory University
Yu-Sheng Chen
University of Chicago https://orcid.org/0000-0002-7646-7761
Tianquan Lian
Emory University https://orcid.org/0000-0002-8351-3690
Yurii Geletii
Department of Chemistry/Emory Univ
Djamaladdin Musaev
Emory University https://orcid.org/0000-0003-1160-6131
John Bacsa
Emory University

Article

Keywords: multi-electron catalysts, molecular water oxidation catalyst, [Co2Ni2(PW9O34)2]10- (Co2Ni2P2), electronic structure tuning

Posted Date: September 21st, 2021

DOI: https://doi.org/10.21203/rs.3.rs-785515/v1

Abstract

Mixed 3d-metal oxides are some of the most promising water oxidation catalysts (WOCs), but it is very difficult to know the active site structures and thus structure-catalytic activity correlations at the molecular level in such insoluble materials. This study reports a molecular water oxidation catalyst, $[Co_2Ni_2(PW_9O_{34})_2]^{10-}$ ($Co_2Ni_2P_2$), that constitutes a molecular model of the heterogeneous WOC, cobalt-nickel oxide. Both $Co_2Ni_2P_2$ and its isostructural analogue, $[Co_4(PW_9O_{34})_2]^{10-}$ (Co_4P_2), have the same $CoO_5(H_2O)$ active sites but $Co_2Ni_2P_2$ is an order of magnitude faster than Co_4P_2. $Co_2Ni_2P_2$ is prepared by a new synthesis, and both the location and percent occupancy of Co and Ni in $Co_2Ni_2P_2$ (Co outside and Ni inside the central belt are >97% for each) is confirmed by multiwavelength synchrotron X-radiation anomalous dispersion scattering (synchrotron XRAS), a technique applied for the first time to such complexes. Density functional theory (DFT) studies predicated and reveal that Co_4P_2 and $Co_2Ni_2P_2$ have greatly altered frontier orbitals, while stopped-flow kinetic studies and DFT calculations indicate that water oxidation by both complexes follows analogous multi-step mechanisms, including Co-OOH formation, with the energetics of most steps being lower for $Co_2Ni_2P_2$ than for Co_4P_2.

Introduction

Efficient and sustained catalytic water oxidation remains a central challenge in the production of solar fuel. There is a voluminous recent literature on homogeneous and heterogeneous WOCs,[1–11] including transition-metal-substituted polyoxometalates (POMs) that have been used in both modes, as soluble complexes amenable to extensive molecular-level characterization, and as components of photoanodes.[7, 8, 12–22] POM complexes have become popular as WOCs because their structures and compositions can be extensively altered synthetically, yet they share the oxidative stability, low-cost and scalability of earth-abundant-element, heterogeneous metal oxide WOCs.[23–26]

Many WOC studies probe the detailed molecular processes at or adjacent to the transition-metal active site that facilitate the four-electron, four-proton process of water oxidation (Eq. 1) including identification of oxidation states and potentials of the active site metals and ligand atoms likely involved in the mechanism.[4, 5]

$$2H_2O\ (\text{liquid}) \rightarrow 4e + 4H^+ + O_2\ (\text{gas}) \quad (1)$$

However, there are no studies to our knowledge that assess the impact on catalytic water oxidation and WOC stability of perturbing the electronic structure of the active site by a neighboring redox-active transition metal while keeping constant the rest of the catalytic transition-metal active-site structure. This active site includes all the ligands that impact electron transfer (ET and PCET) events, counterion association, and oxygen-oxygen bond formation. The pK_a values of ligands proximal to the redox-active transition-metal active site would also ideally be kept constant. In this context, our aim was to take the much studied sandwich-type POM water oxidation catalyst, **Co_4P_2**, (Figure 1a)[7, 15, 16, 21] and devise a way

to replace the two internal, solvent-inaccessible metals in the central belt (the two internal Co(II) centers in **Co_4P_2**), with another redox-active transition metal, then quantify the impact of this isomorphous, isostructural and iso-charge replacement on the properties, including but not limited to the catalytic water oxidation turnover rate, on the exposed active-site cobalt centers. This requires a new synthesis leading to the first sandwich POMs with two different transition metals installed selectively at different sites. We focus on **$Co_2Ni_2P_2$** (Figure 1b) which contains two nickels in place of the internal cobalts in the parent WOC, **Co_4P_2** (Figure 1a), as this would be a molecular model of Co-Ni mixed oxide, one of the most effective heterogeneous WOCs known.[6, 27, 28] At the same time, the active-sites in **$Co_2Ni_2P_2$** and those in **Co_4P_2** would have essentially congruent cobalt-active-site geometries, both having $Co(H_2O)(POM\text{-}oxygen)_5$ octahedra with very similar bond distances, angles and negative charge densities (both **$Co_2Ni_2P_2$** and **Co_4P_2** polyanions bear a 10- charge in their resting oxidation states). The only difference in the two WOCs is the phenomenon we are targeting – isostructural replacement of the internal transition metals in the central belt with another transition metal. Since the internal Ni(II) centers in the central belt of **$Co_2Ni_2P_2$** are buried, they can't participate directly in the bond breaking and forming steps in water oxidation: they have no open coordination positions to bind H_2O, H^+, various intermediates or O_2. These central Ni(II) centers, however, can in principle, impact the catalysis and other properties, such as the nature and energies of the frontier orbitals, the hydrolytic stability, and the spectroscopy of these POM WOCs.

We report here a general synthesis of POM WOCs with two precisely located proximal redox-active transition metals and give a 3-step synthesis of **$Co_2Ni_2P_2$**. We introduce the use of multiwavelength synchroton X-radiation anomalous dispersion scattering (synchrotron XRAS)) experiments for the first time to POM studies, and show that this technique unequivocally confirms the implications of several other experiments that only 2 Co(II) and 2 Ni(II) atoms reside in the outside and inside central-belt positions of **$Co_2Ni_2P_2$**. DFT calculations reveal the profound impact of the Ni-for-Co replacement on electronic structure, and a range of studies show enhanced WOC activity in **$Co_2Ni_2P_2$** relative to **Co_4P_2** and other impacts of this new type of selective WOC modification. An ensemble of computational and experimental results facilitate formulation of a mechanism for the oxidation of water oxidation to O_2 catalyzed by **$Co_2Ni_2P_2$**.

Results And Discussion

Synthesis of two-transition-metal sandwich POMs. The strategy for making this unprecedented type of POM involves 3 steps (Fig. 2). All 3 POM structures in Fig. 2 are the X-ray structures. Reaction with the sodium salt of both tungstate and phosphate with nickel nitrate yields the structural analogue of **Co_4P_2**, namely $[Na_2(Ni)_2(PW_9O_{34})_2]^{12-}$ (**$Na_2Ni_2P_2$**), a complex with exchangeable sodium centers on the outside of the central belt, and Ni(II) centers installed in the internal, buried positions. The occupancy of the Na and Ni centers is confirmed by single crystal X-ray diffraction because Na and Ni(II) have sufficiently different electron densities.[29] In the second step, treatment of **$Na_2Ni_2P_2$** with Co(II) salts ($CoCl_2$ works

satisfactorily) at pH 5.5 in the presence of KCl, forms **$Co_2Ni_2P_2$** in good yield but with $[Co(H_2O)_6]^{2+}$ counterions. These counter-cations refine well crystallographically and are evident in Fig. 2 (lower left structure). However, these counter-cations must be removed because hydrated divalent cobalt ions form multi-cobalt polyhydroxo complexes that are very good WOCs and would thus interfere with comparison of the activities of **$Co_2Ni_2P_2$** and other WOCs. The third step involves slow re-crystallization from concentrated (0.27 M) KCl which replaces the $[Co(H_2O)_6]^{2+}$ counter-cations with redox-inactive K^+ ones. The single crystal X-ray diffraction (*vide infra*), elemental analysis (Table S1) and the TGA results indicate that the complete structural formula of the ion-exchanged complex (after step 3), including final crystallization, is a mixed potassium, sodium salt: $K_8Na_2Co_2Ni_2P_2W_{18}O_{68}{\bullet}30H_2O$ (KNa**$Co_2Ni_2P_2$**; see Methods section).

Structures. The X-ray crystal structures of **$Co_2Ni_2P_2$** both with and without $[Co(H_2O)_6]^{2+}$ counterions (Fig. 2; lower left and lower right, respectively) reveal that the **$Co_2Ni_2P_2$** polyanion consists of two trivacant B-α-$[PW_9O_{34}]^{9-}$ Keggin moieties with four 3d transition metals in the central belt, the classical sandwich polyanion structure first reported by Weakley et al. in 1972[30] and appearing in scores of publications since. The refinement strongly suggests that this central belt contains two chemically equivalent Ni(II) centers in the internal positions of this C_i symmetry polyanion and two chemically equivalent Co(II) centers in the external, solvent accessible positions defining a rhomb-like Co_2Ni_2 tetrad (Fig. 1b and Fig. 2 bottom structures). Each Co^{2+} ion in **$Co_2Ni_2P_2$** coordinates to six oxygen atoms of the two B-α-$[PW_9O_{34}]^{9-}$ units.

Infrared spectra of conventional and two-metal sandwich POMs. To assess if FTIR spectra could distinguish these two classes of sandwich POMs, the conventional polyanion with the same four transition metals in the central belt of the complex, from the new, two-transition-element sandwich POMs, the FTIR spectra of **Co_4P_2** and **$Co_2Ni_2P_2$** in the P-O, W-O, and W-O-W stretch regions were compared (Figure 3). These regions are very similar, strongly suggesting that the two complexes are isostructural to one another overall. However, the triply degenerate v_3 vibrational mode of the central PO_4 unit in **Co_4P_2** is broadened but not split; whereas, it is split in **$Co_2Ni_2P_2$** and in the $(\text{alkali metal})_2(\text{transition metal})_2$ precursor complex, **$Na_2Ni_2P_2$**, indicating a greater structural distortion and a consequent lowering of the symmetry around this central heteroatom unit in the latter two polyanions. The peaks in the low energy ($<1000\ cm^{-1}$) region are attributed to the characteristic $\nu(W\text{-}O_d)$, $\nu(W\text{-}O_b\text{-}W)$ and $\nu(W\text{-}O_c\text{-}W)$ absorptions, where O_b = double-bridging oxygen; O_c = central oxygen; and O_d = terminal oxygen.

Synchrotron XRAS: confirmation of metal positions and occupancies. While the single crystal X-ray structure of **$Co_2Ni_2P_2$**, supported by FTIR spectral and elemental analysis data, suggests the presence of a CoNiNiCo sequence in the central belt of the complex, this structural assignment was uncertain because Co and Ni have very similar electron densities (Z values). Unequivocally and quantitatively distinguishing between adjacent 3d elements in the periodic table in a structure that also contains 18 heavily-scattering tungsten ions as in **$Co_2Ni_2P_2$**, is particularly problematical even with recent

conventional X-ray diffractometers equipped with strong X-ray sources and improved detectors. Since the thrust of this study is the impact of changing the internal 3d transition metal adjacent to the water-oxidizing external transition metals on the properties of this WOC, the unequivocal confirmation of this CoNiNiCo structural sequence is imperative. As a consequence, we turned to the use of synchrotron XRAS data to address this conundrum, and while not applied previously to POM systems, is ideally suited to quantify both the location and the abundance of the two belt-transition-metals, Co and Ni, in **$Co_2Ni_2P_2$**. This technique should also be definitive for structural assignments in myriad potential multiple-transition-metal-containing catalysts for the multi-electron processes central to solar fuel production, HER, OER (WO) and carbon dioxide reduction (CO_2RR).

The basis of the XRAS technique, details of its application to this dual-transition-metal identification problem and data collection are given in the SI. Measurements, made at the Advanced Photon Source, were acquired over a wide range of wavelengths that included the two K-edges of cobalt and nickel. Data collections were displaced at either side of the two K-edges (Figure S1). Use of the program GSAS-II[31] facilitate use of all the multiple wavelength data to refine the populations of cobalt and nickel atoms at these specific metal sites. High-resolution data (30 keV) gave us an optimal structural model for the refinement of the fractions of both metals. The results are presented in Table 1. In short, the Co(II) and Ni(II) centers are confirmed to be located in 97% and 96% in the outer, solvent-accessible, and inner solvent-inaccessible positions of the central belt of **$Co_2Ni_2P_2$**, respectively (Fig. 1b).

Table 1. GSAS-II refinement results of $Na_2K_8Co_2Ni_2P_2W_{18}O_{68}{\bullet}30H_2O$

Outer M atoms	Inner M atoms
Co 0.97(1) Ni 0.03(1)	Ni 0.96(1) Co 0.04(1)

Catalyzed water oxidations by a sacrificial electron acceptor.

The catalytic efficiency of **Co_4P_2**, **Ni_4P_2**, **$Na_2Ni_2P_2$** and **$Co_2Ni_2P_2$** for water oxidation was evaluated in dark homogeneous, photodriven homogeneous and electrocatalytic conditions. The dark reactions used $[Ru(bpy)_3](ClO_4)_3$ as a stoichiometric oxidant, Eq. 2, and were monitored by the UV-Vis spectroscopic kinetics of $[Ru(bpy)_3]^{3+}$ (ε_{670} = 420 M^{-1} cm^{-1})[32] consumption in 80 mM borate buffer at pH 8.0 using the stopped-flow technique.

$$4[Ru(bpy)_3]^{3+} + 2H_2O \rightarrow 4[Ru(bpy)_3]^{2+} + O_2 + 4H^+ \quad (2)$$

Typical kinetic curves, shown in Figure 4, are not exponential. The addition of 1.0 μM **$Co_2Ni_2P_2$** results in almost complete $[Ru(bpy)_3]^{3+}$ consumption in less than 0.5 s, which is an order of magnitude faster than with 1.0 μM **Co_4P_2** and more than 60 times faster than the self-decomposition rate of $[Ru(bpy)_3]^{3+}$, also shown in Figure 4. For comparison, we also recorded the kinetics of $[Ru(bpy)_3]^{3+}$ reduction catalyzed by 5

μM $Co(NO_3)_2$ (brown) and by 5 μM **$Na_2Ni_2P_2$**(green). The oxygen yields, based on the initial concentration of the oxidant, $[Ru(bpy)_3^{3+}]$, increase with catalyst concentrations and reach a plateau of about 70-80% at 5.0 μM catalyst (**$Co_2Ni_2P_2$** or **Co_4P_2**). In the presence of **Ni_4P_2** or **Na_2Ni_2P**, the rate of $[Ru(bpy)_3]^{3+}$ consumption is the same as in the absence of a catalyst.

Light-driven catalytic water oxidation

The activity of **$Co_2Ni_2P_2$** in visible-light-driven catalytic water oxidation was assessed using a standard approach with $[Ru(bpy)_3]Cl_2$ as the photosensitizer and persulfate, $Na_2S_2O_8$, as a sacrificial electron acceptor (Figure 5).[33, 34] The initial rate of O_2 formation is commonly, but incorrectly, considered as a direct measure of the catalytic activity, but in actuality this slope is a measure of the initial quantum yield. Under the conditions in Figure 5, the O_2 yields and quantum yields in the presence of **$Co_2Ni_2P_2$**are reproducibly ~23% higher than those of in the presence of **Co_4P_2**. The O_2 yields in the **Ni_4P_2** and **$Na_2Ni_2P_2$** reactions are the same as those without a catalyst.The light-induced oxidative decomposition of the photosensitizer, $[Ru(bpy)_3]^{2+}$, by persulfate is the mainside-reaction in the absence of a water oxidation catalyst.

Stability of the Co $_2$ Ni $_2$ P $_2$ water oxidation catalyst in solution. Four different experiments address that the stability of the catalyst are below. All the details, including considerations and controls for each, are in the SI:

1. **$Co_2Ni_2P_2$** was extracted by tetra-*n*-heptylammonium (THpA)NO_3 from the post-reaction solution into toluene. The aqueous layer was evaluated by cathodic adsorptive stripping voltammetry to quantify the amount of Co(II) from POM decomposition. The concentration of Co(II) in NaBi buffer (100 mM, pH = 8.0) and NaPi buffer (100 mM, pH = 8.0) was 5% and 10%. These concentrations are significantly too low for the observed catalytic activity of **$Co_2Ni_2P_2$**.[35, 36]

2. The concentration of Co(II) present in **$Co_2Ni_2P_2$** solutions was also determined by ^{31}P NMR line broadening analysis. We found that the decomposition of 5 μM **$Co_2Ni_2P_2$** to Co(II) after 1 h in 0.1 M NaPi at pH 8.0 did not exceed 14%.[37, 38]

3. The dependence of catalytic activity on the storage time of **$Co_2Ni_2P_2$** in stock solution in 160 mM NaBi buffer at pH 8.0 was measured by stopped flow kinetics analysis (Figure S11). After 1 h of storage, the activity of **$Co_2Ni_2P_2$** didn't change, again suggesting the significant hydrolytic stability of **$Co_2Ni_2P_2$** in borate buffer at pH 8.0.

4. The addition of bipyridine (bpy) to the solution of Co_{aq}^{2+} results in the formation of mono-, bis, and tris-bpy complexes of Co(II) with $\log_{10}(\beta_i)$ values of 5.65, 11.25, and 16.05.[39] In the solution of 1.0 μM of Co^{2+} and 9.0 μM of bpy, the concentration of free Co^{2+} is lower than 0.02 μM. The addition of small

amounts of bpy to the Co^{2+}-catalyzed water oxidation (H_2O + $[Ru(bpy)_3]^{3+}$) completely shuts down the reaction. If 9.0 μM of bpy is added to the reaction catalyzed by 1.0 μM of $\mathbf{Co_2Ni_2P_2}$, only a very small decrease of $[Ru(bpy)_3]^{3+}$ consumption is observed (Fig. 4). This confirms that Co(II) can't be the true catalyst in the $\mathbf{Co_2Ni_2P_2}$ solution. However, because the bpy ligand notably destabilizes the $\mathbf{Co_2Ni_2P_2}$ POM framework (removes Co(II)) as it does in the case of $\mathbf{Co_4V_2}$,[38] and unlike in the case of $\mathbf{Co_4P_2}$,[36] the addition of 40 μM bpy results in a visible inhibition of the reaction.

Electrocatalytic water oxidation. Previous studies showed that prolonged exposure to the high overpotential conditions required for electrochemical water oxidation tends to decompose cobalt-containing Keggin-sandwich POMs by electrodepositing cobalt oxide species on the working electrode.[35, 36, 38, 40] Embedding Co-POM WOCs in carbon paste has been reported to greatly reduce the hydrolytic decomposition of these catalysts.[41, 42] However, short timescale homogeneous cyclic voltammetry experiments illuminate aspects of the catalytic water oxidation activity of $\mathbf{Co_2Ni_2P_2}$. At 1.0 μM this POM produces a rising anodic current from the catalytic oxidation of water with no corresponding reductive current (Figure 6). More importantly, atom equivalent concentrations of aqueous Co^{2+} and Ni^{2+} (2.0 μM each) result in a lower oxidative currents. Given that aqueous Co^{2+} is a known active WOC (active WOC precursor) and Ni^{2+} is not, this observation strongly suggests that $\mathbf{Co_2Ni_2P_2}$ is a much faster WOC than Co^{2+}. These results are also consistent with the stopped-flow kinetic studies, where we see not only a much faster initial rate of reaction associated with $\mathbf{Co_2Ni_2P_2}$ but also a delayed reaction onset for aqueous Co^{2+} that is nonexistent in the early-time water oxidations catalyzed by POM WOCs.

Comparison of catalytic activity of $Co_2Ni_2P_2$ and Co_4P_2

In order to explain the order of magnitude higher WOC activity of $\mathbf{Co_2Ni_2P_2}$ compared to $\mathbf{Co_4P_2}$, we studied in detail the kinetics of catalytic $[Ru(bpy)_3]^{3+}$ consumption. First, we attempted to estimate the standard reduction potentials of these POMs. The common electrochemical technique does not work in this case. Neither POMs show any electroactive redox behavior prior to their water oxidation catalytic current. Consequently, we performed potentiometric titration by $[Ru(bpy)_3]^{3+}$ (E = 1.26 V) using a stopped flow technique and measuring the $[Ru(bpy)_3]^{2+}$ concentration at 450 nm ($\varepsilon = 1.42 \times 10^4\ M^{-1}cm^{-1}$). The stock solution used for titration was a mixture of $[Ru(bpy)_3]^{3+}$ and $[Ru(bpy)_3]^{2+}$ in a 6:1 ratio. The addition of 0.8-3.0 equivalents of $[Ru(bpy)_3]^{3+}$ to 50 μM of either $\mathbf{Co_2Ni_2P_2}$ or $\mathbf{Co_4P_2}$ resulted in an immediate (after 0.01 s) increase of absorbance at 450 nm due to a presence of $[Ru(bpy)_3]^{2+}$ in a stock solution. The absorbance grows exponentially with a $k \approx 0.15\ s^{-1}$. The rate constant of $[Ru(bpy)_3]^{3+}$ self-decomposition is between 0.02–0.025 s^{-1}. Therefore, the self-decomposition cannot be ignored, and as a compromise, we measured the concentration of $[Ru(bpy)_3]^{2+}$ 2.0 s after mixing in the titration procedure. In the presence of 50 μM $\mathbf{Co_2Ni_2P_2}$, the yield of $[Ru(bpy)_3]^{2+}$ formed was about 15–20% of added

$[Ru(bpy)_3]^{3+}$ (Figure S12). Correspondingly, the first oxidation potential of $\mathbf{Co_2Ni_2P_2}$ must be 20–40 mV higher than that of $[Ru(bpy)_3]^{3+}$. Similar results, within experimental error, were obtained for titration of $\mathbf{Co_4P_2}$.

Based on this finding, we constructed a kinetic model for the catalytic reduction of $[Ru(bpy)_3]^{3+}$. We rule out a sequential oxidation of these POMs by 4 electrons for three reasons: (a) commonly, the oxidation potentials increase with the number of removed electrons, even with redox leveling; (b) both $\mathbf{Co_2Ni_2P_2}$ and $\mathbf{Co_4P_2}$ already have high first Co(III)/Co(II) potentials, and (c) $[Ru(bpy)_3]^{3+}$ is unlikely to be able to remove three additional electrons sequentially. Therefore, we assume that two molecules of $[Ru(bpy)_3]^{3+}$ oxidize one POM to form a 2-electron-oxidized intermediate, which then reacts with water. The resulting peroxy-like species is rapidly oxidized subsequently by two $[Ru(bpy)_3]^{3+}$ to form O_2 and regenerate the initial form of the POM. The simplified kinetic model is Eqs. 3–6:

$$POM + [Ru(bpy)_3]^{3+} \Delta POM(1) + [Ru(bpy)_3]^{2+} \Delta G1 \quad (3)$$

$$POM(1) + [Ru(bpy)_3]^{3+} \Delta POM(2) + [Ru(bpy)_3]^{2+} \Delta G2 \quad (4)$$

$$POM(2) \rightarrow HO\text{-}O\text{-}CoPOM \; k_c \quad (5)$$

$$HO\text{-}O\text{-}CoPOM + 2\,[Ru(bpy)_3]^{3+} \rightarrow POM + 2\,[Ru(bpy)_3]^{2+} + O_2 \text{ fast} \quad (6)$$

Where POM(1) and POM(2) are the one- and two-electron oxidized forms of the initial POM catalyst, and HO-O-CoPOM represents the key cobalt-peroxy intermediate in the rate-determining step.

The self-decomposition of $[Ru(bpy)_3]^{3+}$ is a complex process. The decay of absorbance at 670 nm is exponential, but the yield of $[Ru(bpy)_3]^{2+}$ product is higher than 95% based on initial $[Ru(bpy)_3]^{3+}$. Bpy self-decomposition in oxidative processes has been thoroughly studied in previous work which shows that the oxidatively damaged bpy ligand, bpy', which is almost always more electron-rich than bpy itself, is easily oxidized to CO_2.[32] To take into account the stoichiometry of bpy self-decomposition, we add the reactions 7 and 8 to the kinetic model

$$[Ru(bpy)_3]^{3+} \rightarrow [Ru(bpy')(bpy)_2]^{2+} \text{ self-decomposition} \quad (7)$$

Analysis of this model affords the following values (details of fitting procedure and results are described in the SI) for $\mathbf{Co_2Ni_2P_2}$ ($\mathbf{Co_4P_2}$):

$$\Delta G1 = 29\ (21)\ mV,\ \Delta G2 = -34\ (-33)\ mV,\ k_c = 1.1e+3\ (20)\ s^{-1} \quad (8)$$

Thus, the main reason for the significant difference in catalytic activity between the two POMs seems to be the difference in rates of Eq. 5, which includes O-O bond formation.

To support this hypothesis, we performed quantum-chemical calculations of the thermodynamic properties of the $\mathbf{Co_2Ni_2P_2}$and $\mathbf{Co_4P_2}$ intermediates, which are most likely involved in the catalytic cycle. The details are described in SI. The simplified energy diagram is presented in Fig.7. Accordingly, the difference in activity between these POMs derives primarily from the more favorable thermodynamics of the peroxo (O-O) forming step for $\mathbf{Co_2Ni_2P_2}$than for $\mathbf{Co_4P_2}$. This is analogous to the rate-determining step proposed in other 3d-metal-oxide-based oxidations[43 – 45]

One key insight from the computations is that the inner and outer metal atoms in the central belt of the POM are strongly antiferromagnetically coupled via superexchange (through the bridging oxo ligands) rather than via direct exchange. Specifically, the second order interaction energy of a bonding Co-O orbital with an inner Co d-orbital lone-pair is ~ 0.5 kcal/mol in $\mathbf{Co_4P_2}$, while the same interaction of a bonding Co-O orbital with an inner Ni d-orbital lone-pair is ~ 1.7 kcal/mol. This critical difference in the indirect inner metal-outer metal interaction energies explains, at least in part, the observed difference in the reaction rates between $\mathbf{Co_2Ni_2P_2}$ and $\mathbf{Co_4P_2}$.

Conclusions

This study reports the structural, electronic and reactivity (catalytic turnover rate) impact of changing a redox-active center proximal to the transition metal catalytic active site in a multi-electron catalyst without changing the other active site ligands, ligand coordination sphere geometry, or charge on the catalyst. Specifically, the two Co(II) centers in the internal positions of the four-transition-metal central belt of the water oxidation catalyst, $[Co_4(PW_9O_{34})_2]^{10-}$ ($\mathbf{Co_4P_2}$) were replaced by two Ni(II) centers using a new stepwise, selective-transition-metal replacement approach to yield $[Co_2Ni_2(PW_9O_{34})_2]^{10-}$ ($\mathbf{Co_2Ni_2P_2}$).

• Conventional single-wavelength X-ray crystallographic determination could not unequivocally distinguish two adjacent 3d elements in the presence of many proximal heavy atoms: 18 tungsten centers in the case of $\mathbf{Co_2Ni_2P_2}$. In contrast, multiwavelength synchrotron X-radiation anomalous dispersion scattering (synchrotron XRAS) successfully proved that Co(II) and Ni(II) had been incorporated in 97% and 96% selective occupancies in the outside (Co) and internal (Ni) positions, respectively in $\mathbf{Co_2Ni_2P_2}$.

• This new type of modification resulted in (a) an increase in the catalytic water oxidation turnover rate by an order of magnitude, (b) a lowering of the barrier of 2 of the 3 key steps before and including the rate-limiting step from a kinetic model of the mechanism based on stopped flow kinetics, DFT calculations and optical spectra, and (c) a change in the electronic nature of the frontier orbitals. The interaction between the catalytic outside (solvent-accessible) Co centers and the proximal internal, buried transition metal is quite different for the latter being Co(II) versus Ni(II).

• Similar isomorphous replacements of electronically interacting redox-active centers proximal to active site metal(s) in WOCs and likely catalysts for other multi-electron processes (e.g. H_2O and CO_2 reduction)

are possible and could well have similar impacts on catalyst electronic structure and associated turnover rates.

Methods

General Methods and Materials. All common laboratory chemicals were reagent grade, purchased from commercial sources, and used without further purification. The FT-IR spectra were measured on a Thermo Nicolet 6700 spectrometer. Elemental analyses were performed by Galbraith Lab Inc., Knoxville, TN, 37921. Thermogravimetric (TGA) data were collected on an Instrument Specialists Incorporated TGA 1000 instruments.

Co(II) in buffered catalytic solutions. By convention, Co(II) in aqueous solution is denoted as "Co^{2+}" or "$[Co(H_2O)_6]^{2+}$"; however, divalent cobalt in the borate and phosphate buffers used to control pH in the catalysis and stability studies in this paper, replace some of aqua ligands bound to cobalt, thus writing "$Co(H_2O)_6]^{2+}$" in the buffered solution studies is somewhat misleading. As a consequence, we write divalent cobalt in this paper as "Co(II)" for these studies which encompasses the different hydrolysis and association species of cobalt. The Co(II)-buffer association equilibria are discussed and where possible quantified in the Supporting Information (SI).[46, 47] In contrast, writing "$[Co(H_2O)_6]^{2+}$" is appropriate for the syntheses and X-ray crystallographic studies where all 6 aqua ligands of the cobalt counterions are confirmed.

Synthesis of $K_8Na_4[Na_2Ni_2(PW_9O_{34})_2]\cdot 30H_2O$ ($Na_2Ni_2P_2$).[29] $Na_2WO_4 \cdot 2H_2O$ (5 g, 15.2 mmol) and Na_2HPO_4 (0.24 g, 1.7 mmol) were dissolved in 50 mL of H_2O followed by the addition of $Ni(NO_3)_2 \cdot 6H_2O$ (0.32 g, 1.1 mmol), resulting in a cloudy suspension. The pH was adjusted to 7.5 by dropwise addition of 6 M HCl, and a yellow-green solution formed. The solution was heated at 90 ^oC for 1 h and then was allowed to cool to room temperature. Powdered KCl (0.6 g, 8.0 mmol) was added, and the solution was allowed to evaporate for several days at room temperature generating 0.2 g of yellow-green needles (7% yield based on W).

Synthesis of $K_{10}[Co_2Ni_2(PW_9O_{34})_2]\cdot 28H_2O$ ($K_{10}Co_2Ni_2P_2$). $Na_2Ni_2P_2$ (0.04 g) was dissolved in 4 mL of 1 M $CoCl_2$ aqueous solution. KCl (0.08 g in 1 mL of solution) was added under stirring at 50 °C to accelerate the crystallization. Dark purple-brown crystals with two $[Co(H_2O)_6]^{2+}$ as counterions to the deca-anion, $Co_2Ni_2P_2$, were obtained overnight upon slow evaporation (0.028 g, 70 % yield). The two $[Co(H_2O)_6]^{2+}$ counterions were quantitatively removed by recrystallization as follows: 5 mg of the above crystals were dissolved in 4 mL of water, and 1 mL of KCl solution (0.1 $g \cdot mL^{-1}$) was added under stirring at 50 °C. Single crystals suitable for X-ray crystallography were obtained overnight upon slow evaporation (yield 2.5 mg, 50%). FTIR data (cm^{-1}): 1039(s), 1012(s), 936(sh), 889(sh), 700(s). The TGA measurement indicated 30 water molecules of crystallization. Elemental analysis calcd (wt%) for $Co_2Ni_2P_2$: Co, 2.22; Ni, 2.21; P, 1.15; W, 62.46; Found (wt%): Co, 2.00; Ni, 2.11; P, 1.04; W, 61.70.

The POMs, $Na_{10}[Co_4(H_2O)_2(PW_9O_{34})_2]\cdot 27H_2O$ (**Co_4P_2**) and $Na_6K_4[Ni_4(H_2O)_2(PW_9O_{34})_2]\cdot 32H_2O$ (**Ni_4P_2**), for control experiments were synthesized by the literature procedures.[15, 48]

X-ray structure of the POMs. These routine determinations are described in the SI and in the available CIF file.

XRAS Experiments. Standard, single-wavelength X-ray diffraction is generally not sensitive enough to unequivocally distinguish neighboring transition-metal atoms in the periodic table in a molecule. This is particularly true where there are many adjacent heavy atoms, as in the case of **$Co_2Ni_2P_2$** which contains 18 tungsten atoms. Synchrotron XRAS proved to be ideal for this purpose. Key aspects of the technique pertaining to **$Co_2Ni_2P_2$** are in the Results and Discussion below, and the technical basics and scattering details are given in the SI. Six data sets were collected at the Advanced Photon Source (15-ID-B) using radiation close to the K-edges of cobalt and nickel to unequivocally determine the exact nature of these metal atoms in the central belt of **$Co_2Ni_2P_2$**. Specifically, measurements were performed at and displaced at either side of the K-edges of Co (1.608 Å, 7.71 keV) and Ni (1.488 Å, 8.33 keV). The conditions available at 15-ID-B enabled collection of extremely high-resolution, multi-wavelength and complete data sets that are responsive to the exact composition of the Co/Ni atom sites in the crystal.

Evaluation of catalytic activity. The catalytic activity towards water oxidation was evaluated using the techniques described earlier[16, 33] and also addressed below. The O_2 yield in water oxidation by $[Ru(bpy)_3]^{3+}$ was measured in a custom-built apparatus, that was described in detail earlier.[49] The oxygen concentration was measured by an Ocean Optics Neofox Phase Measurement System containing a calibrated FOXY-R probe with a FOXY-AFMG coating. The measurements were performed until the oxygen reading was constant for 3-5 consecutive experiments. Analysis of oxygen in the reaction headspace in the light-driven system was performed using a HP7890A model gas chromatograph (GC) equipped with thermal conductivity detector (TCD) and a 5Å molecular sieve capillary column. The kinetics and the O_2 yields in this system are strongly dependent on the stirring rate, light intensity, configuration of a light source and reactor.[16, 36] Therefore, this technique is applicable only for determining the relative catalytic activities of different complexes under strictly identical conditions.

Computational details. Here, we used the M06L density functional[50] in conjuction with the 6-31G(d,p) basis sets for P, O and H atoms, and LANL2DZ ECPs with the corresponding basis sets for W, Co, and Ni. The effects of bulk aqueous solution were approximated at the level of the polarizable continuum model (PCM).[51] Roles of the long-range dispersion interactions were evaluated using the GD3 method.[52] Geometry optimizations of all structures were done without symmetry constraints and at their energetically lowest high-spin states. All the calculations were performed using Gaussian 09 (Revision E.01) quantum chemical software package[53] (for more details see the Supporting Information).

Declarations

Acknowledgments

This work was supported by the US Department of Energy, Office of Basic Energy Sciences, Solar Photochemistry Program (DE-FG02-07ER15906) to C.L.H., T.L. and D.G.M. The authors gratefully acknowledge the resources of the Cherry Emerson Center for Scientific Computation – NSF MRI-R2 grant (CHE-0958205).

References

1. Concepcion JJ, *et al.* Making Oxygen with Ruthenium Complexes. *Acc Chem Res* **42**, 1954–1965 (2009).
2. Eisenberg R, Gray HB. Preface on Making Oxygen. *Inorg Chem* **47**, 1697–1699 (2008).
3. Eisenberg R. Rethinking Water Splitting. *Science* **324**, 44–45 (2009).
4. Kärkäs MD, Verho O, Johnston EV, Åkermark B. Artificial Photosynthesis: Molecular Systems for Catalytic Water Oxidation. *Chem Rev* **114**, 11863–12001 (2014).
5. Blakemore JD, Crabtree RH, Brudvig GW. Molecular Catalysis for Water Oxidation. *Chem Rev* **115**, 12974–13005 (2015).
6. McCrory CCL, Jung S, Ferrer IM, Chatman SM, Peters JC, Jaramillo TF. Benchmarking Hydrogen Evolving Reaction and Oxygen Evolving Reaction Electrocatalysts for Solar Water Splitting Devices. *J Am Chem Soc* **137**, 4347–4357 (2015).
7. Lauinger SM, Yin Q, Geletii YV, Hill CL. Polyoxometalate Multielectron Catalysts in Solar Fuel Production. In: *Advances in Inorganic Chemistry: Volume 69. Polyoxometallate Chemistry* (eds Cronin L, Eldik Rv). 1st edn. Elsevier, Oxford, UK (2017).
8. Li J, Güttinger R, Moré R, Song F, Wan W, Patzke GR. Frontiers of water oxidation: the quest for true catalysts. *Chem Soc Rev* **46**, 6124–6147 (2017).
9. Mondschein JS, *et al.* Crystalline Cobalt Oxide Films for Sustained Electrocatalytic Oxygen Evolution under Strongly Acidic Conditions. *Chem Mater* **29**, 950–957 (2016).
10. Lyons MEG, Doyle RL, Browne MP, Godwin IJ, Rovetta AAS. Recent developments in electrochemical water oxidation. *Current Opinions in Electrochemistry* **1**, 40–45 (2017).
11. Song F, *et al.* An Unconventional Iron Nickel Catalyst for the Oxygen Evolution Reaction. *ACS Cent Sci* **5**, 558–568 (2019).
12. Geletii YV, Botar B, Kögerler P, Hillesheim DA, Musaev DG, Hill CL. An All-Inorganic, Stable, and Highly Active Tetraruthenium Homogeneous Catalyst for Water Oxidation. Selected as the VIP Article by the reviewers and editor. *Angew Chem Int Ed* **47**, 3896–3899 (2008).
13. Sartorel A, *et al.* Polyoxometalate Embedding of a Tetraruthenium(IV)-oxo-core by Template-Directed Metalation of $[\gamma\text{-}SiW_{10}O_{36}]^{8-}$: A Totally Inorganic Oxygen-Evolving Catalyst. *J Am Chem Soc* **130**, 5006–5007 (2008).

14. Geletii YV, *et al.* Structural, Physicochemical and Reactivity Properties of an All-Inorganic, Highly Active Tetraruthenium Homogeneous Catalyst for Water Oxidation. *J Am Chem Soc* **131**, 17360–17370 (2009).
15. Yin Q, *et al.* A fast soluble carbon-free molecular water oxidation catalyst based on abundant metals. *Science* **328**, 342–345 (2010).
16. Huang Z, *et al.* Efficient Light-Driven Carbon-Free Cobalt-Based Molecular Catalyst for Water Oxidation. *J Am Chem Soc* **133**, 2068–2071 (2011).
17. Toma FM, *et al.* Efficient Water Oxidation at Carbon Nanotube–Polyoxometalate Electrocatalytic Interfaces. *Nat Chem* **2**, 826–831 (2010).
18. Carraro M, *et al.* Artificial Photosynthesis Challenges: Water Oxidation at Nanostructured Interfaces. *Top Curr Chem* **303**, 121–150 (2011).
19. Car P-E, Guttentag M, Baldridge KK, Albertoa R, Patzke GR. Synthesis and characterization of open and sandwich-type polyoxometalates reveals visible-light-driven water oxidation *via* POM-photosensitizer complexes. *Green Chem* **14**, 1680–1688 (2012).
20. Mukhopadhyay S, Debgupta J, Singh C, Kar A, Das SK. A Keggin Polyoxometalate Shows Water Oxidation Activity at Neutral pH: POM@ZIF-8, an Efficient and Robust Electrocatalyst. *Angew Chem Int Ed* **57**, 1918–1923 (2018).
21. Liu B, *et al.* Cobalt-to-vanadium charge transfer in polyoxometalate water oxidation catalysts revealed by 2p3d resonant inelastic X-ray scattering. *Phys Chem Chem Phys* **20**, 4554–4562 (2018).
22. Martin-Sabi M, *et al.* Redox tuning the Weakley-type polyoxometalate archetype for the oxygen evolution reaction. *Nature Catalysis* **1**, 208–213 (2018).
23. Okuhara T, Mizuno N, Misono M. Catalytic Chemistry of Heteropoly Compounds. *Adv Catal* **41**, 113–252 (1996).
24. Hill CL. Introduction: Polyoxometalates—Multicomponent Molecular Vehicles To Probe Fundamental Issues and Practical Problems. *Chem Rev* **98**, 1–2 (1998).
25. Borrás-Almenar JJ, Coronado E, Müller A, Pope MT. *Polyoxometalate Molecular Science. Proceedings of the NATO Advanced Study Institute, Tenerife, Spain from 25 August to 4 September 2001*. Kluwer Academic Publishers (2003).
26. Long D-L, Tsunashima R, Cronin L. Polyoxometalates: Building Blocks for Functional Nanoscale Systems. *Angew Chem Int Ed* **49**, 1736–1758 (2010).
27. Smith RDL, *et al.* Photochemical Route for Accessing Amorphous Metal Oxide Materials for Water Oxidation Catalysis. *Science* **340**, 60–63 (2013).
28. Trotochaud L, Boettcher SW. Precise Oxygen Evolution Catalysts: Status and Opportunities. *Scripta Materialia* **74**, 25–32 (2014).
29. Hou Y, Xu L, Cichon MJ, Lense S, Hardcastle KI, Hill CL. A New Family of Sandwich-Type Polytungstophosphates Containing Two Types of Metals in the Central Belt: $M'_2M_2(PW_9O_{34})_2^{12-}$ (M' = Na or Li, M = Mn^{2+}, Co^{2+}, Ni^{2+},and Zn^{2+}). *Inorg Chem* **49**, 4125–4132 (2010).

30. Weakley TJR, Evans HT, Jr., Showell JS, Tourné GF, Tourné CM. 18-Tungstotetracobalto(II)diphosphate and related Anions: a Novel Structural Class of Heteropolyanions. *J Chem Soc, Chem Commun* **4**, 139–140 (1973).
31. Toby BH, Dreele RBV. GSAS-II: the genesis of a modern open-source all purpose crystallography software package *J Appl Crystallography* **46**, 544–549 (2013).
32. Ghosh PK, Brunschwig BS, Chou M, Creutz C, Sutin N. Thermal and Light-Induced Reduction of $Ru(bpy)_3^{3+}$ in Aqueous Solution. *J Am Chem Soc* **106**, 4772–4783 (1984).
33. Geletii YV, Huang Z, Hou Y, Musaev DG, Lian T, Hill CL. Homogeneous Light-Driven Water Oxidation Catalyzed by a Tetraruthenium Complex with All Inorganic Ligands. *J Am Chem Soc* **131**, 7522–7523 (2009).
34. White HS, Becker WG, Bard AJ. Photochemistry of the Tris(2,2'-bipyridine)ruthenium(II)-Peroxydisulfate System in Aqueous and Mixed Acetonitrile-Water Solutions. Evidence for a Long-Lived Photoexcited Ion Pair. *J Phys Chem* **88**, 1840–1846 (1984).
35. Stracke JJ, Finke RG. Electrocatalytic Water Oxidation Beginning with the Cobalt Polyoxometalate $[Co_4(H_2O)_2(PW_9O_{34})_2]^{10-}$: Identification of Heterogeneous CoO_x as the Dominant Catalyst. *J Am Chem Soc* **133**, 14872–14875 (2011).
36. Vickers JW, *et al.* Differentiating Homogeneous and Heterogeneous Water Oxidation Catalysis: Confirmation that $[Co_4(H_2O)_2(\alpha\text{-}PW_9O_{34})_2]^{10-}$ Is a Molecular Water Oxidation Catalyst. *J Am Chem Soc* **135**, 14110–14118 (2013).
37. Folkman SJ, Kirner JT, Finke RG. Cobalt Polyoxometalate $Co_4V_2W_{18}O_{68}^{10-}$: A Critical Investigation of Its Synthesis, Purity, and Observed ^{51}V Quadrupolar NMR. *Inorg Chem* **55**, 5343–5355 (2016).
38. Sullivan KP, *et al.* Speciation and Dynamics in the $[Co_4V_2W_{18}O_{68}]^{10-}$/ $CO(II)_{aq}$ / CoC_x Catalytic Water Oxidation System. *ACS Catal* **8**, 11952–11959 (2018).
39. *Critical Stability Constants: First Supplement*. Springer US (1982).
40. Lv H, *et al.* An Exceptionally Fast Homogeneous Carbon-free Cobalt-based Water Oxidation Catalyst. *J Am Chem Soc* **136**, 9268–9271 (2014).
41. Blasco-Ahicart M, Soriano-López J, Carbó JJ, Poblet JM, Galan-Mascaros JR. Polyoxometalate electrocatalysts based on earth-abundant metals for efficient water oxidation in acidic media. *Nat Chem* **10**, 24–30 (2018).
42. Arens JT, *et al.* Water oxidation electrocatalysis in acidic media with Co-containing polyoxometalates. *J Catal* **389**, 345–351 (2020).
43. Haschke S, *et al.* Direct oxygen isotope effect identifies the rate-determining step of electrocatalytic OER at an oxidic surface *Nat Commun* **9**, 1–8 (2018).
44. Dau H, Limberg C, Reier T, Risch M, Roggan S, Strasser P. The Mechanism of Water Oxidation: From Electrolysis via Homogeneous to Biological Catalysis. *ChemCatChem* **2**, 724–761 (2010).

45. Man IC, *et al.* Universality in Oxygen Evolution Electrocatalysis on Oxide Surfaces. *ChemCatChem* **3**, 1159–1165 (2011).
46. Richens DT. *The Chemistry of Aqua Ions: Synthesis, Structure, and Reactivity: A Tour through the Periodic Table of the Elements*. John Wiley & Sons (1997).
47. Abu-Shandi K, Al-Wedian F. Estimation of composition, coordination model, and stability constant of some metal/phosphate complexes using spectral and potentiometric measurements. *Chem Papers* **63**, 420–425 (2009).
48. Lv H, *et al.* A Noble-Metal-Free, Tetra-nickel Polyoxotungstate Catalyst for Efficient Photocatalytic Hydrogen Evolution. *J Am Chem Soc* **136**, 14015–14018 (2014).
49. Vickers JW, Sumliner JM, Lv H, Morris M, Geletii YV, Hill CL. Collecting meaningful early-time kinetic data in homogeneous catalytic water oxidation with a sacrificial oxidant. *Phys Chem Chem Phys* **16**, 11942–11949 (2014).
50. Zhao Y, Truhlar DG. A new local density functional for main-group thermochemistry, transition metal bonding, thermochemical kinetics, and noncovalent interactions. *The Journal of Chemical Physics* **125**, 194101 (2006).
51. Barone V, Cossi M. Quantum Calculation of Molecular Energies and Energy Gradients in Solution by a Conductor Solvent Model. *The Journal of Physical Chemistry A* **102**, 1995–2001 (1998).
52. Grimme S, Antony J, Ehrlich S, Krieg H. A consistent and accurate ab initio parametrization of density functional dispersion correction (DFT-D) for the 94 elements H-Pu. *The Journal of Chemical Physics* **132**, 154104 (2010).
53. Frisch MJ, *et al.* Gaussian 09 Revision E.01.) (2013).

Figures

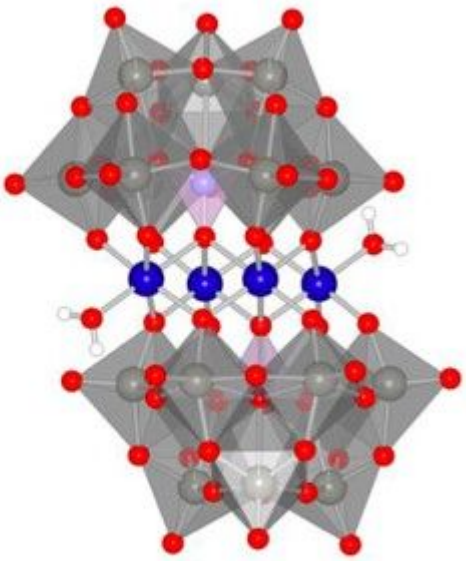

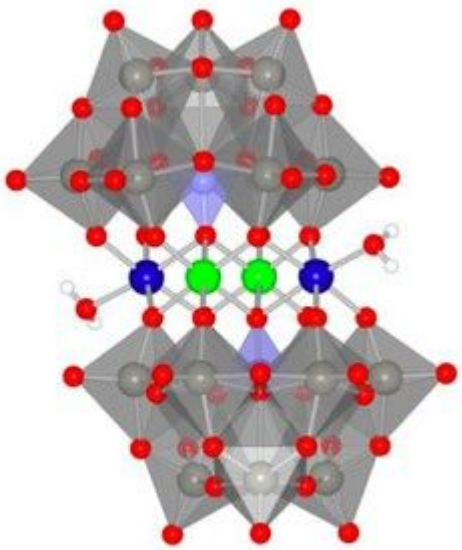

Figure 1

Structures of polyoxometalate water oxidation catalysts that have the same cobalt active site structures, overall structures, and molecular charges: Co4P2 and Co2Ni2P2. Co: blue; Ni: green; WO6, gray octahedra.

Figure 2

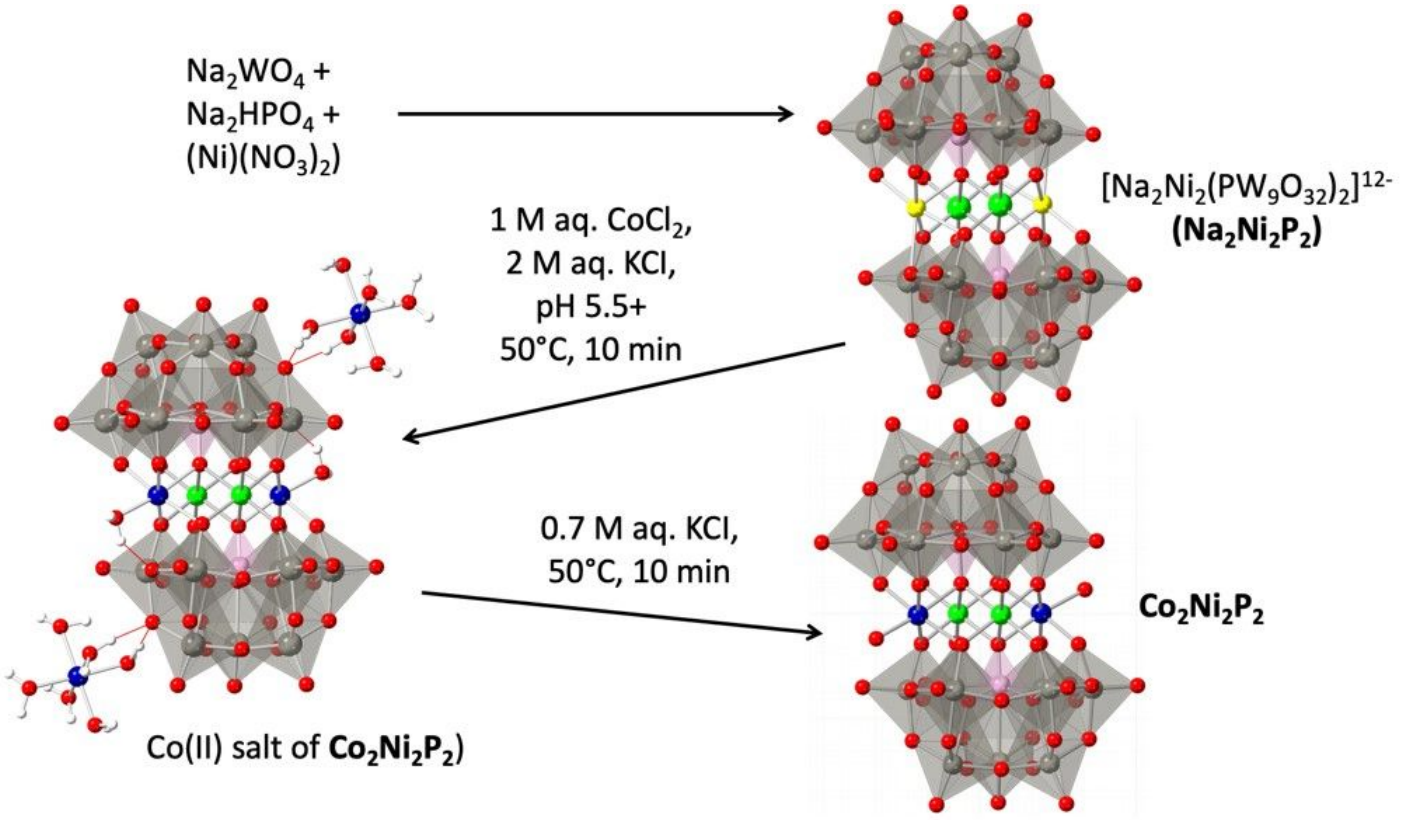

Synthesis of a two-transition-metal POM water oxidation catalysts.

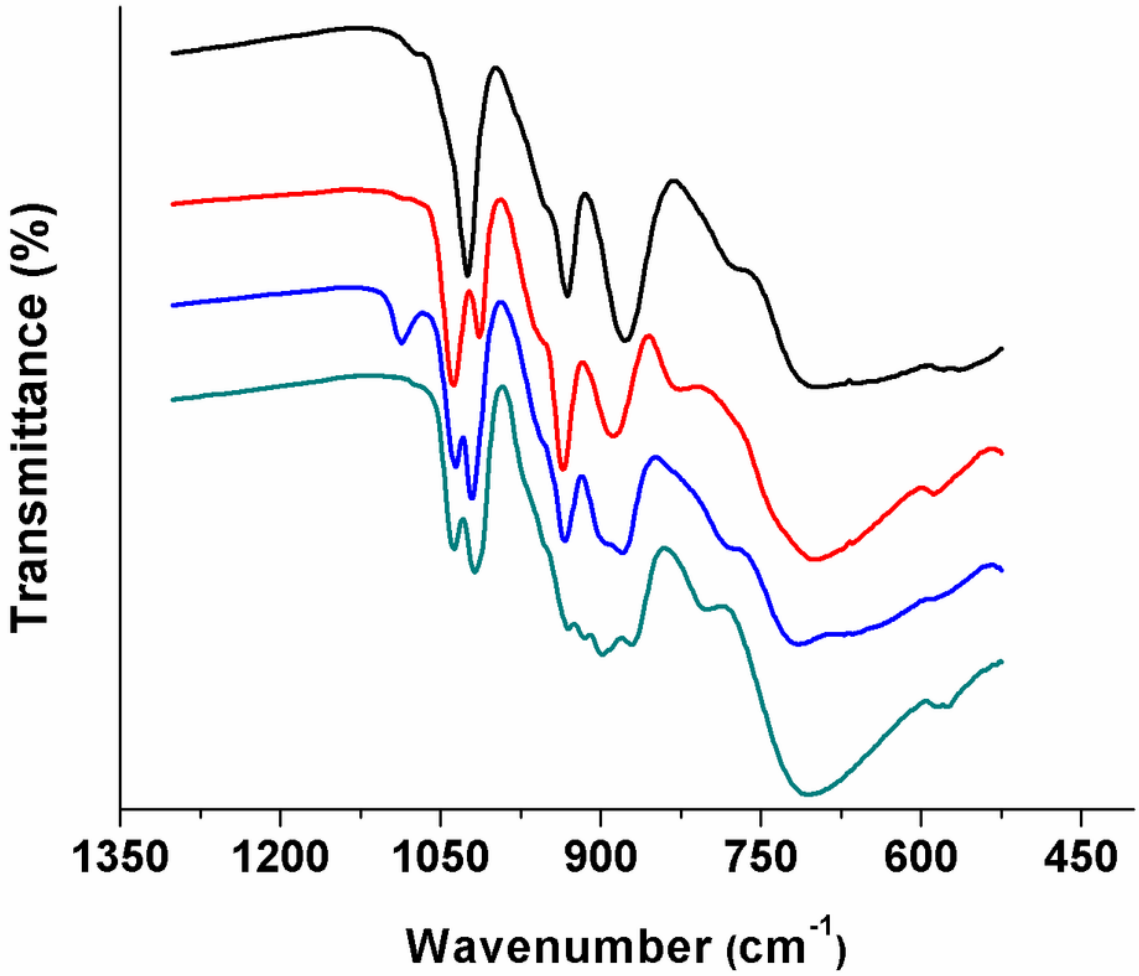

Figure 3

Comparison of FTIR spectra Co4P2 (black), Co2Ni2P2 (red), Ni4P2 (blue) and Na2Ni2P2 (green).

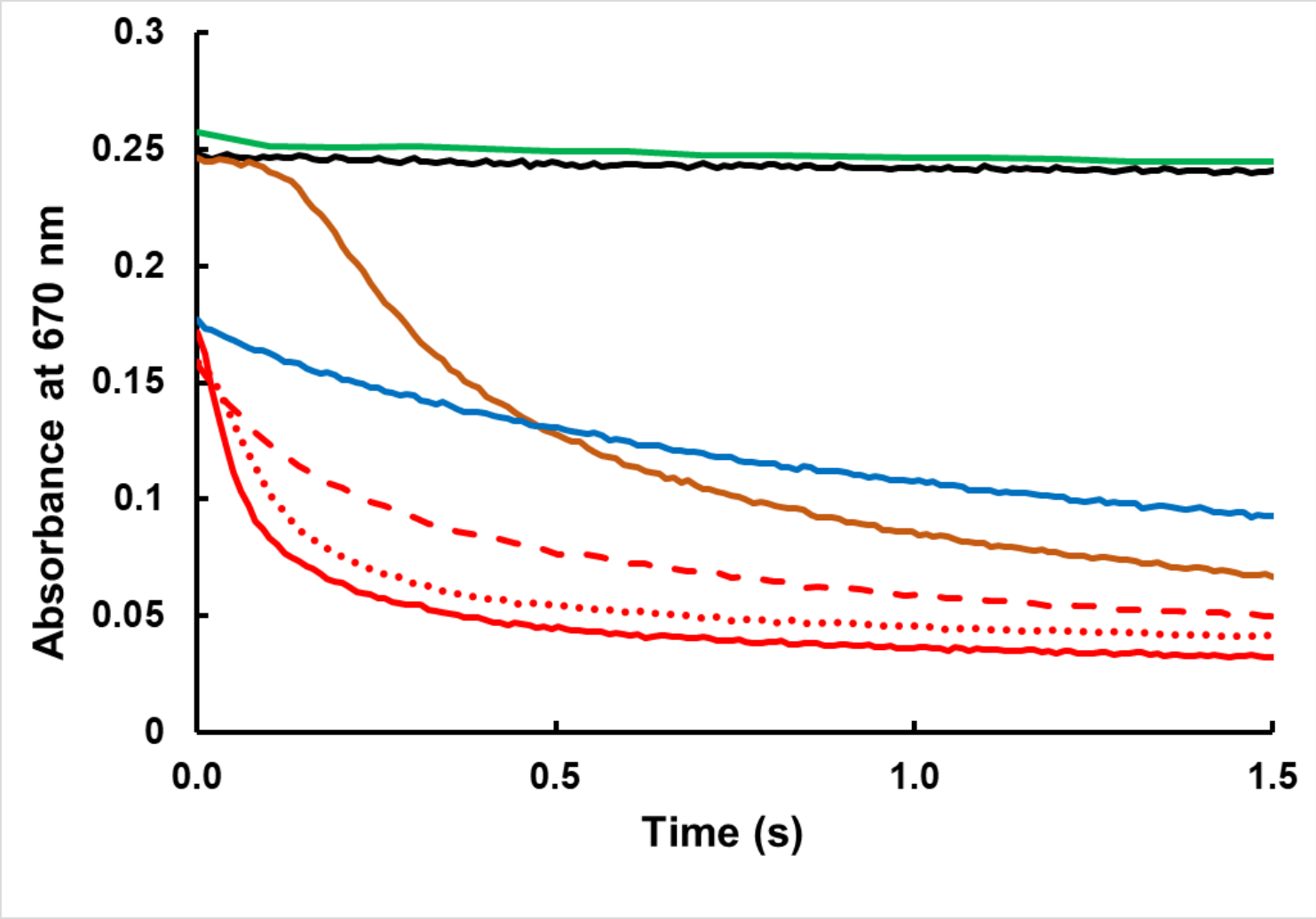

Figure 4

Kinetics of [Ru(bpy)3]3+ reduction measured as the decrease in absorbance at 670 nm. Black - no catalyst, green - 5 μM Na2Ni2, brown - 5 μM Co(NO3)2, blue - 1 μM Co4P2, red - 1 μM Co2Ni2P2 with 0 (solid), 9 μM bpy (dotted), 40 μM bpy (dashed); Conditions: 0.43 mM (red and blue) or 0.6 mM [Ru(bpy)3]3+ (brown, black, and green), 80 mM sodium borate buffer at pH 8.0, 298 K.

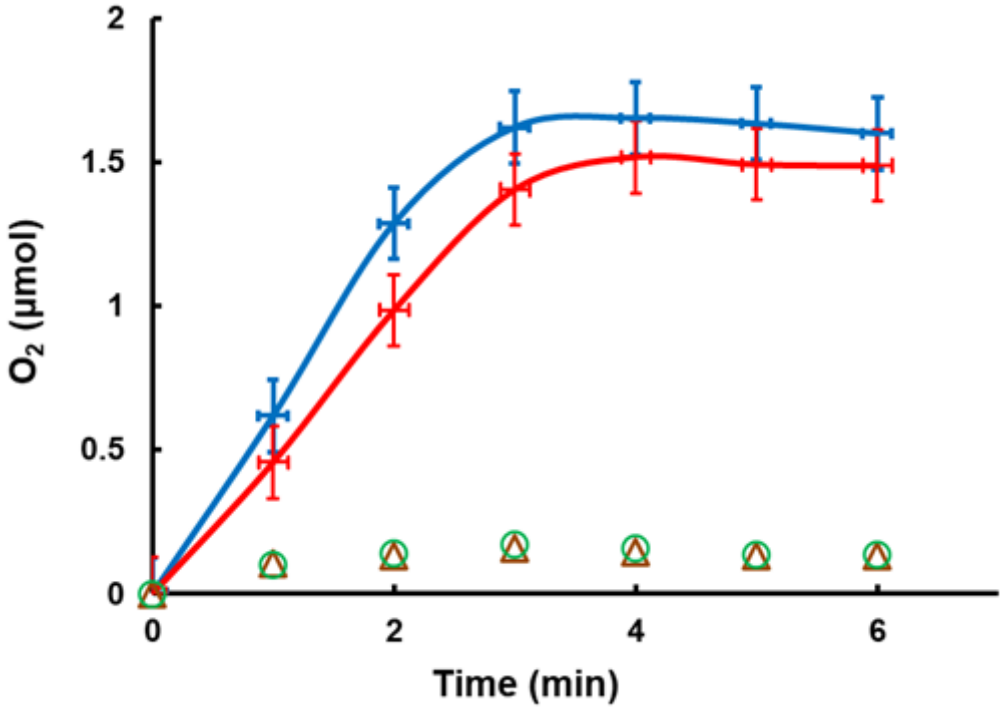

Figure 5

Kinetics of O2 evolution in the light driven reactions with 1.0 mM [Ru(bpy)3]Cl2 and 5.0 mM Na2S2O8 catalyzed by 10 µM of Co2Ni2P2 (blue), Co4P2 (red), Ni4P2 (green), and Na2Ni2P2 (brown). Conditions: 455 nm LED light (17 mW, beam diameter ca. 0.4 cm), 80 mM sodium borate buffer, initial pH 8.0, total solution volume 2.0 mL.

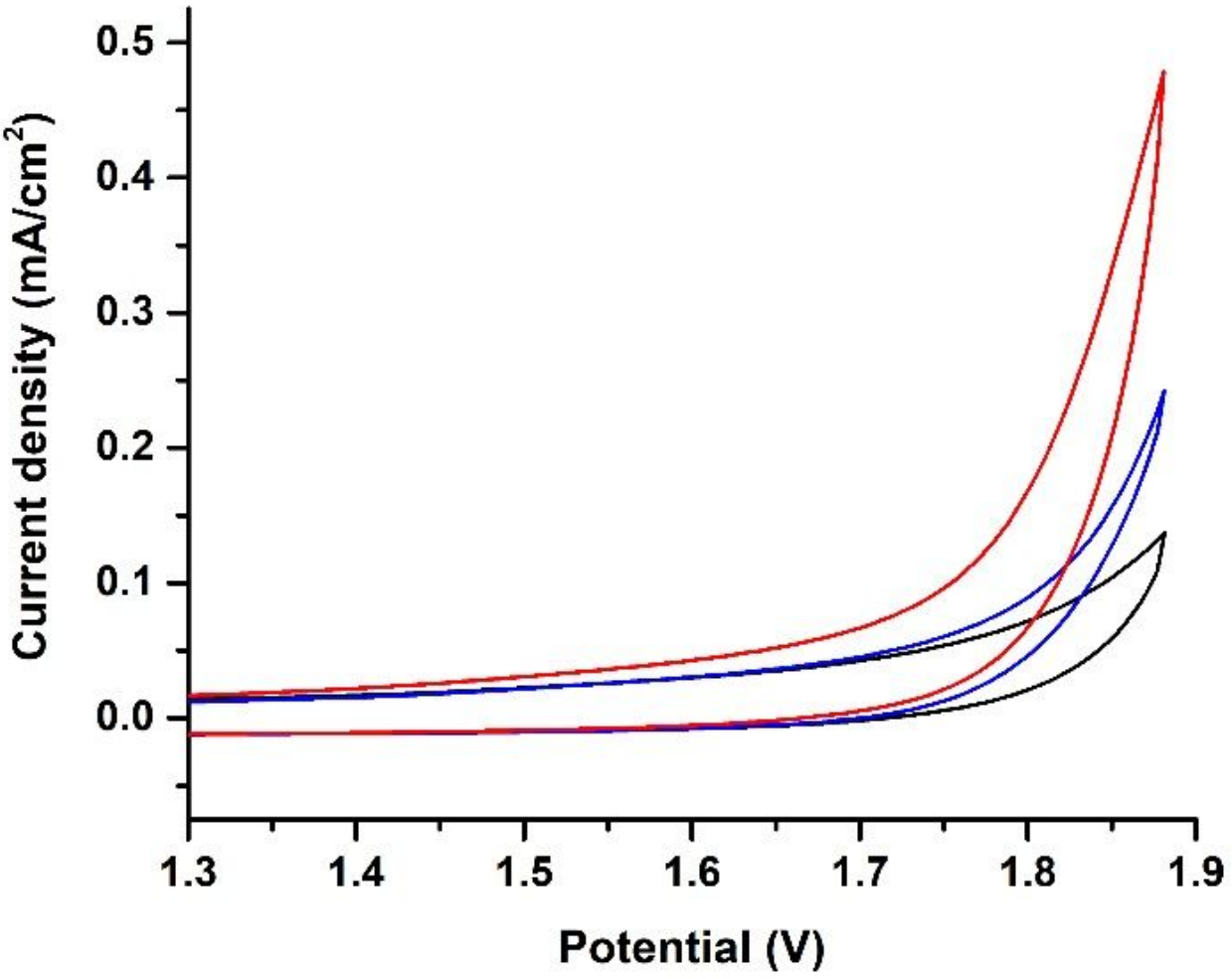

Figure 6

Cyclic voltammetry of different catalytic species. No catalyst (black), 1.0 μM Co2Ni2P2 (red), and 2.0 μM Co(NO3)2 + 2.0 μM Ni Co(NO3)2 (blue). Conditions: 0.1 M pH 8.0 borate buffer with 0.1 M of KNO3 as the electrolyte; glassy carbon working electrode; Ag/AgCl reference electrode; 50 mV/s scan rate. The plotted potential is based on the reversible hydrogen electrode.

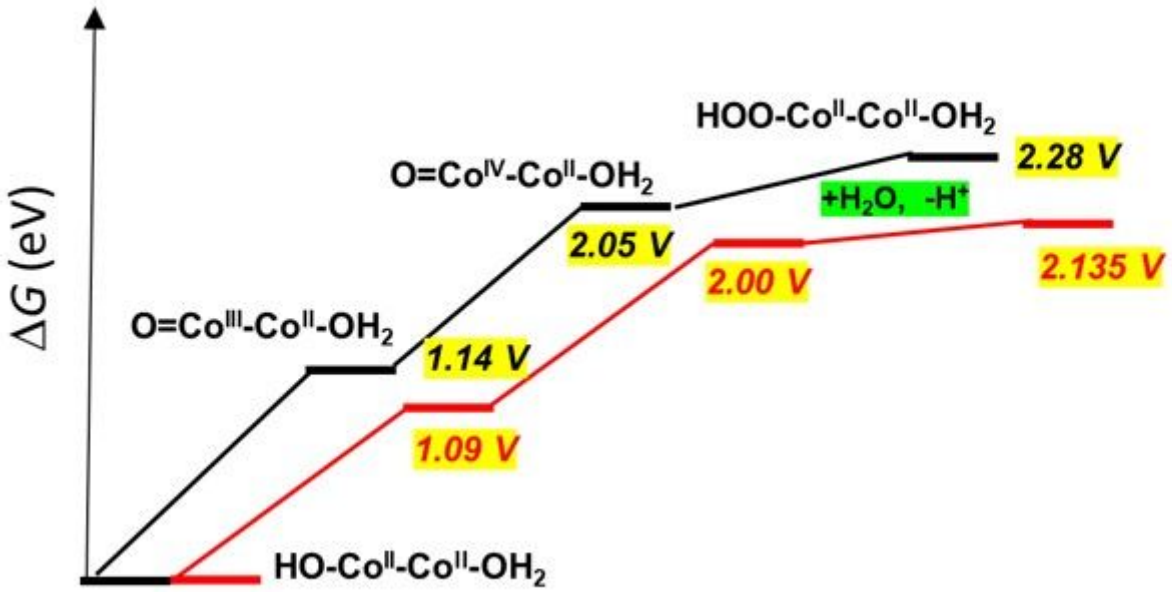

Figure 7

Calculated thermodynamics of the CoO-OH hydroperoxo and other intermediates that form with Co2Ni2P2 (red) and Co4P2 (black).

Supplementary Files

This is a list of supplementary files associated with this preprint. Click to download.

- SINewTypeofWaterOxidationCatalyst.docx